



Modeling studies of the coastal circulation off Northern California: shelf response to a major Eel river flood event

Julie D. Pullen^{*,1}, J.S. Allen

College of Oceanic and Atmospheric Sciences, Oregon State University, Corvallis, OR, 97331, USA

Abstract

The region surrounding Cape Mendocino is the subject of a high-resolution multiply nested modeling study. The highest resolution model (1 km) is used for a 40-day simulation containing the major Eel River flood event of December 30, 1996–January 3, 1997. The complex forcing due to rapidly shifting storm-driven winds, flood-induced river discharge and rugged bathymetry and coastline generate energetic coastal circulation off northern California during this time. The Eel River plume mixes significantly in the down-stream direction and influences the velocity structure of the shelf flow. Coastline irregularities are important in generating an eddy over the Eel River margin through the establishment of an alongshore pressure gradient. Time series and statistics of the modeled alongshore velocity field show good agreement with observed values at the S60 and G65 ADCP sites. © 2000 Elsevier Science Ltd. All rights reserved.

Keywords: Coastal circulation; Northern California; Plume dynamics; Numerical modeling

1. Introduction

The northern California shelf region experienced several severe storms in winter 1996–1997. The discharge from precipitation-laden rivers caused major flooding in early January 1997 throughout the region, during which time the Eel River (40.6°N, 124.3°W) experienced an 80-yr flood event (Syvitski and Morehead, 1999). The Strata Formation on Margins (STRATAFORM) observational program instrumented the region north of the Eel River during the flood season. The focus of that program is to understand the transport and accumulation of sediments on

*Corresponding author.

¹Currently at Naval Research Laboratory, Monterey, California, USA.

continental margins (Nittrouer, 1999). Geyer et al. (2000) describe the evolution of a plume formed by Eel River outflow during the flood. They discuss characteristics of the plume, as well as construct a budget for the sediment carried by the plume. The flood was caused by a passing cyclonic storm system and as a consequence, the coastal region was subjected to strong poleward (downwelling-favorable) winds followed by equatorward (upwelling-favorable) winds. The plume was confined close to the coast and flowed poleward during downwelling-favorable winds. During the subsequent upwelling-favorable winds the plume expanded offshore and thinned vertically. These two plume response patterns to opposing wind conditions have also been documented in observational studies by Rennie et al. (1999) and Münchow and Garvine (1993). As the winds transitioned to upwelling-favorable, the suspended sediment concentration in the plume diminished substantially, indicating sediment fall-out from the plume (Hill et al., 2000). The analysis by Geyer et al. (2000) considered sediment transport by the 5–10 m thick Eel River plume. In particular, their analysis did not directly account for low-frequency shelf circulation that could play a role in determining sediment fate once it sinks out of the plume (Ogston et al., 2000).

Recognized as a source of buoyancy and momentum for the coastal ocean, river run-off has been included in idealized model configurations. Chao (1987) used a primitive equation model and described effects of wind on buoyancy currents. Upwelling winds modified the structure of the current as described above. Fong (1998) extended the work of Chao (1987) by analyzing dynamic river plume responses to upwelling and downwelling winds over a straight coastline. Fong (1998) documented momentum balances and characterized mixing in the river plume for an alongshore-averaged two-dimensional section. Garvine (1999) investigated the dependence of three-dimensional plume characteristics on model parameters.

Recent modeling studies have incorporated realistic forcing, including spatially and temporally varying winds and river run-off (e.g., Kourafalou, 1999; Masson and Cummins, 1999). They demonstrate the role of alongshore variability in the shelf dynamics and compare model results with observations.

The present study reports the results of a 40-day simulation focused on the major Eel River flood event of winter 1996–1997 using a high-resolution nested model with approximately 1-km resolution ($\Delta y = 1.0$ km, $\Delta x = 1.0$ to 1.1 km). We nested a series of local high-resolution models (3- and 1-km resolution, respectively) within a regional model of the North Pacific Ocean (9-km resolution). The Naval Research Laboratory's Pacific West Coast Model (NRL PWC) was used as the regional model (Clancy et al., 1996). The NRL PWC is an implementation of the Princeton Ocean Model (POM), as are all interior nested models. All models utilize 30 vertical sigma levels. POM is a sigma-coordinate primitive equation model with an embedded turbulence scheme (Blumberg and Mellor, 1987). Pullen (2000) contains the details of the nesting approach. In Pullen and Allen (2000), the first nested model (3-km resolution) simulation of 100 days in winter 1996–1997 is used to describe the circulation with and without river run-off. Strong variability and complex flow is characteristic of the northern Eel River margin even in the absence of river run-off. Pullen and Allen (2000) report a robust anticyclonic eddy centered off the Eel River

mouth that occurred in response to the transient wind forcing imposed by passing storms. This eddy is strengthened by river discharge and is a circulation response to the shift of winds from strongly poleward to weakly equatorward. In addition, Pullen and Allen (2000) demonstrate the prevalence of a generic dynamic shelf response to storm events using terms in the depth-integrated alongshore momentum equation. The role of a southward pressure gradient force in assisting current reversal from northward to southward over the shelf is also emphasized by Pullen and Allen (2000).

The present paper will describe the second nested model simulation (1-km resolution). The goal of this work is to characterize the shelf circulation during a 40-day time period surrounding the Eel River flood event, to compare model results with observations during that time period, and to document the Eel River plume interaction with the background shelf flow.

2. Model forcing

The model extends 275 km alongshore and about 125 km offshore (Fig. 1). Bathymetry was generated from the high-resolution Navy DBDB0.5' and DBDB1' (approximately 0.75 and 1.5 km, respectively) digitized data base. The precipitous shelf and slope terrain of the Mendocino Escarpment is well-resolved. Important coastline irregularities, labeled in Fig. 1, are also well-represented by the model resolution.

Wind and river run-off are significant forcing mechanisms in the winter season and are represented realistically in the model simulation (Fig. 2). Navy Operational Global Atmospheric Prediction System (NOGAPS) model wind stresses are used to force the NRL PWC model. Over the 40-day period of simulation the NOGAPS wind stresses agree well with stresses calculated from observed winds at Buoy 46030, hereafter designated Buoy No. 30, adjacent to Cape Mendocino. The correlation coefficient is 0.95, while NOGAPS (observed) mean = 0.99 (0.70) dyn cm^{-2} , and NOGAPS (observed) standard deviation = 1.89 (1.49) dyn cm^{-2} . Therefore, NOGAPS winds are also used to force the nested models.

Low-pass filtered hourly river discharge of the Eel and Klamath rivers from USGS river gauge stations (Fig. 2) is introduced into all model domains by the technique of Kourafalou et al. (1996). The river inlet is three-grid cells wide to match the inlet width on the 3-km domain. The inlet length is five-grid cells. The river mass flux is input at the top vertical level at the innermost grid cells at the head of the inlet. (See Pullen and Allen, 2000, for details of the river implementation.)

After January 2, winds reverse to upwelling-favorable as discharge from the Eel River decreases. By contrast, discharge from the Klamath River remains at peak during this wind relaxation. The abrupt switch from downwelling- to upwelling-favorable winds as the storm passes and the timing of this wind reversal relative to the unsteady river discharge introduces substantial complexity to the shelf circulation. Peak discharge from the Klamath River exceeds that of the Eel River discharge by 5000 m s^{-3} . Nonetheless, due to a variety of factors including the easily

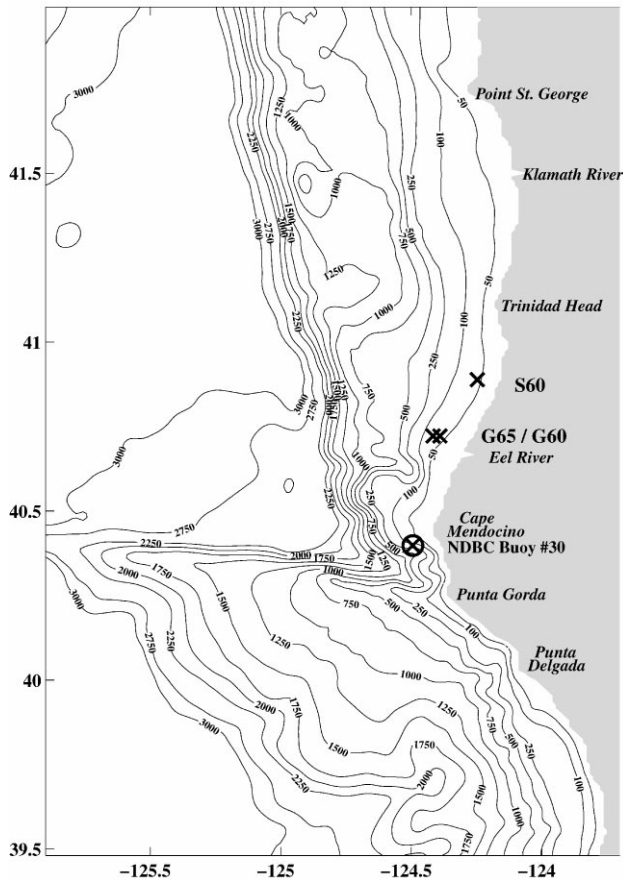


Fig. 1. Domain and bathymetry of the second nested model (1-km resolution). The locations of STRATAFORM data sites G65, G60 and S60 on the shelf are indicated with crosses. The National Data Buoy Center (NDBC) Buoy 46030 (designated Buoy No. 30) located off Cape Mendocino is marked with a circled cross.

erodible rock and steepness of the Eel drainage basin, the Eel River carries the largest sediment load of the California rivers (Sommerfeld and Nittrouer, 1999).

3. Statistics of shelf circulation

The G65 and S60 sites (over the 65 and 60 m isobaths, respectively) on the northern California shelf were instrumented with tripod-mounted RDI workhorse ADCPs during the major January 1997 flood event (Ogston et al., 2000). The sites have an alongshore separation of about 18 km. Here the observations from those instruments are used to assess the performance of the 1- and 3-km model

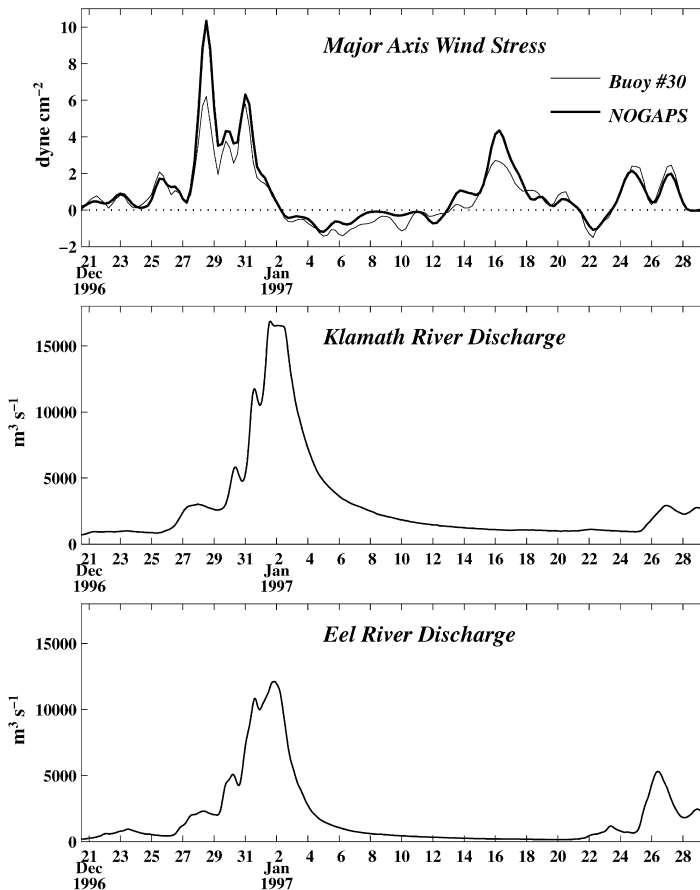


Fig. 2. Model forcing for the NRL PWC and nested models for the 40-day simulation. Model (NOGAPS) wind stress at the location of Buoy No. 30 (40.4°N, 124.5°W), about 30 km south of the Eel River mouth, is shown and compared with wind stress calculated from Buoy No. 30 measured wind speeds (Pullen and Allen, 2000). USGS river gauge discharge values for the Klamath (Turwar station) and Eel Rivers (Scotia and Bridgeville stations combined) are also displayed.

simulations. All modeled and observed values are averaged over an inertial period (18 h) and recorded every 6 h. Modeled and observed velocities are then rotated into the principal axes of the depth-averaged current. This effectively isolates the alongshore (major axis) and across-shore (minor axis) directions when the coastline has a variable orientation.

Observations at the S60 site are described by Ogston et al. (2000). The observed time-mean vertical structure of the major axis (alongshore) current at S60 (Fig. 3) is equatorward during the 32-day period surrounding the flood event. The standard deviation of the observed major axis (alongshore) current varies from 24 cm s^{-1} at 8 m depth to 14 cm s^{-1} at 58 m depth. The 1-km simulation vertical structure of the time-mean alongshore velocity is virtually identical to the observed structure. By

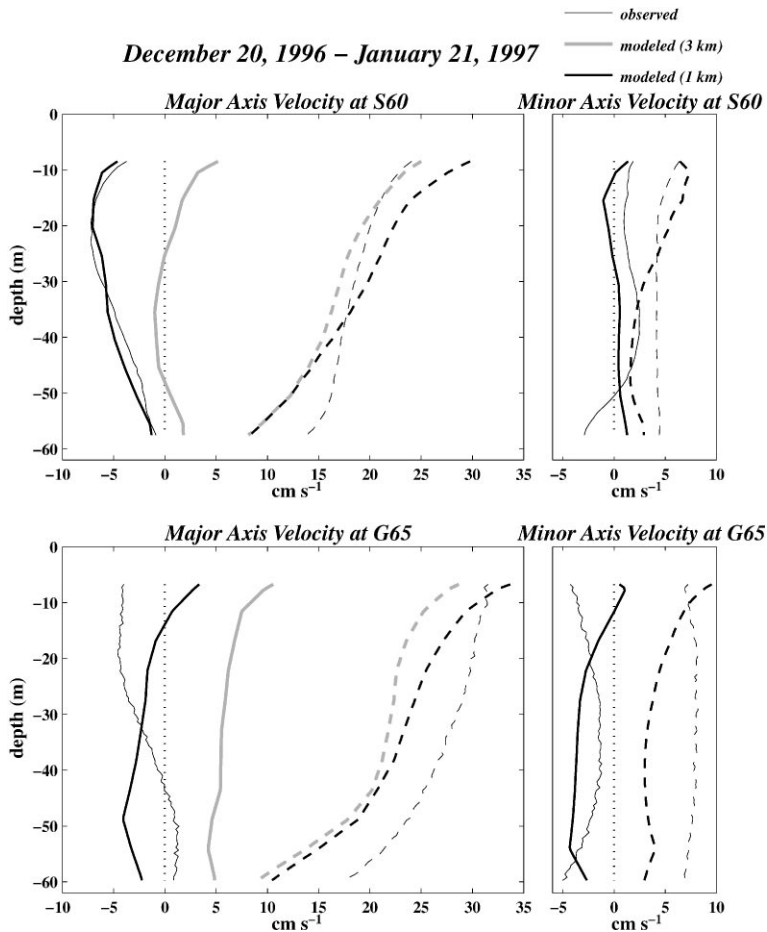


Fig. 3. Observed and modeled vertical structure of the time-mean (solid) and standard deviation (dashed) of major axis (alongshore) velocity at S60 and G65. Statistics are computed over a common overlapping ADCP deployment period of 32 days. The ADCP data are shown courtesy of C. Friedrichs (G65) and A. Ogston (S60).

contrast, the 3-km solution, though accurately tracking the observed S60 time series over 100 days (Pullen and Allen, 2000), does not reproduce the time-mean observed equatorward flow at all depths during the 32-day period. In general, vertical profiles of standard deviation of the model alongshore velocity at the S60 site match the observed shape. In terms of magnitude, both the 3 and 1-km solutions underestimate the variability near the bottom by about 5 cm s^{-1} while the 1-km solution overestimates the variability near the surface by about 5 cm s^{-1} .

The observed time-mean alongshore velocity at the G65 ADCP site is equatorward at most depths (Fig. 3). Observed standard deviation of velocity at 7 m depth is 32 cm s^{-1} while it is reduced to 18 cm s^{-1} at 60 m depth. The velocity

from the 1-km model reproduces the magnitude of the time-mean better than the 3-km model. In addition the 1-km model comes closer to matching the magnitude of observed velocity standard deviation above about 45 m than the 3-km solution. Observed variability is larger at all depths at G65 compared with S60, and the difference between them is greater near the surface than it is at depth. The relative difference in the standard deviation between the two sites is qualitatively represented by both models. However, both models produce smaller standard deviations near the bottom compared with observations. The large spatial variability in mean and fluctuating velocity between G65 and S60 could contribute to discrepancies between the model and observations.

Observed and 1-km modeled minor axis (across-shore) time-mean and standard deviations at S60 and G65 (Fig. 3) are small in comparison to the corresponding major axis quantities. The 3-km model results are qualitatively similar to those from the 1-km model and are not plotted. The 1-km solution time-mean across-shore velocities are small in magnitude, but have differences in vertical structure compared with the observations. In particular, the observed time-mean velocity is onshore at S60 above 52 m depth while the 1-km solution presents a near-zero, depth-independent mean. The observed standard deviation is relatively barotropic in nature, with near-surface standard deviations exceeding those in the rest of the water column by less than 2 cm s^{-1} . Modeled across-shore velocity fluctuations have stronger shear in the vertical than the observed fluctuations.

At G65 the observed across-shore time-mean current is directed off-shore at all depths. Magnitudes of the mean are larger than at the S60 site. Observed standard deviations are twice as large at G65 as they are at S60. The vertical structure of observed fluctuations is barotropic. As at S60, modeled across-shore current mean values have similar magnitudes, but differ in vertical structure, while the standard deviations are somewhat smaller than the observed values and have greater vertical shear. The pronounced differences in observed and simulated across-shelf velocity at the two sites separated by less than 20 km are presumably related to the relatively short alongshore correlation scales of across-shore velocity that are in contrast to the longer correlation scales of the alongshore velocity. The correlation between the S60 and G65 sites of observed minor (major) axis velocity at 30 m depth is -0.22 (0.86), while the 1-km model minor (major) axis velocity correlation between the S60 and G65 sites at 30 m depth is -0.28 (0.83).

The time series of modeled and observed alongshore velocity at G65 (Fig. 4) demonstrate that the 1-km solution reproduces the observed equatorward flow associated with the arrival of equatorward winds better than the 3-km solution. This feature is also found in the S60 time series (not shown) and likely accounts for the difference in mean flow profiles between the 1- and 3-km solutions. Both 1- and 3-km alongshore velocities are highly correlated with the observed velocity. Correlation coefficients are between 0.80 and 0.85 for both the 1- and 3-km models at all three depths. Minor axis (across-shore) correlations of model and observed time series are low and similar for the 1- and 3-km solutions. An exception is at mid-depth (30 m) where the 1-km solution attains a correlation coefficient of 0.56 at S60.

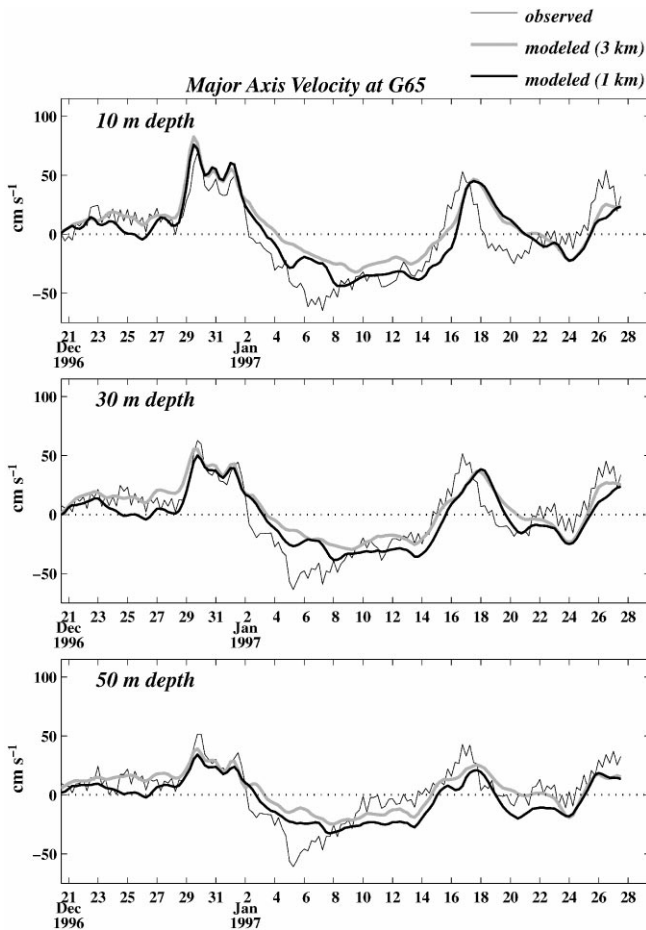


Fig. 4. Time series of modeled and observed major axis (alongshore) and minor axis (across-shore) velocity at three depths at the G65 site. The ADCP data are shown courtesy of C. Friedrichs.

The horizontal spatial structure of the 1-km model time-mean and fluctuating currents is exhibited in maps. Surface current variability is greatest over the northern Eel margin (from the Eel River to Trinidad Head) and north of Point St. George (Fig. 5). Over the 40-day simulation period the magnitude of fluctuations in those regions is typically $40\text{--}50 \text{ cm s}^{-1}$. Time-mean surface velocities are poleward and have magnitudes of about 20 cm s^{-1} over the northern Eel margin and 50 cm s^{-1} north of Point St. George.

The depth-averaged time-mean current is equatorward over the northern Eel margin (Fig. 6). This is in agreement with the depth structure at the measurement locations S60 and G65 (Fig. 3) and extends that result to illustrate the broad horizontal spatial swath of mean equatorward depth-averaged flow. Low-frequency depth-averaged current fluctuations are strong (approximately 20 cm s^{-1}) over the

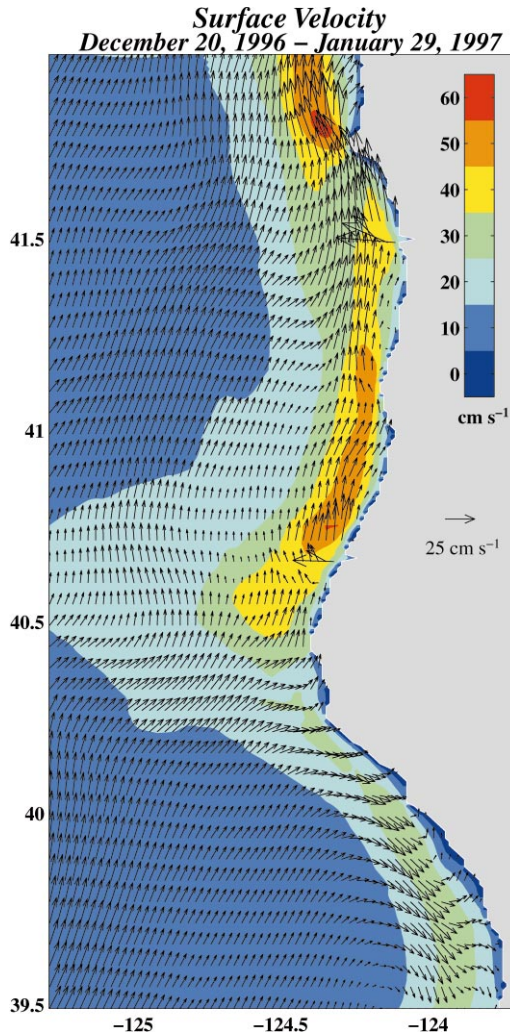


Fig. 5. Surface velocity vector mean and rms vector amplitude of the 1-km resolution model over the 40-day simulation. Means are denoted with arrows, while rms amplitude is color contoured. Every sixth vector alongshore is shown, while every second vector in the across-shore direction is shown. The full north–south extent of the model domain is represented; however, the domain is truncated to the west to highlight the shelf region.

shelf precisely along the stretch of coast, the northern Eel margin, that is the locus of STRATAFORM observations. Thus, STRATAFORM samples a highly energetic flow field relative to the surrounding ocean. Pullen and Allen (2000) found this high variability north of Cape Mendocino to be unrelated to river run-off, though freshwater input increased the magnitude of fluctuations in the surface waters. The localization of maximum variability in discrete regions suggests the influence of

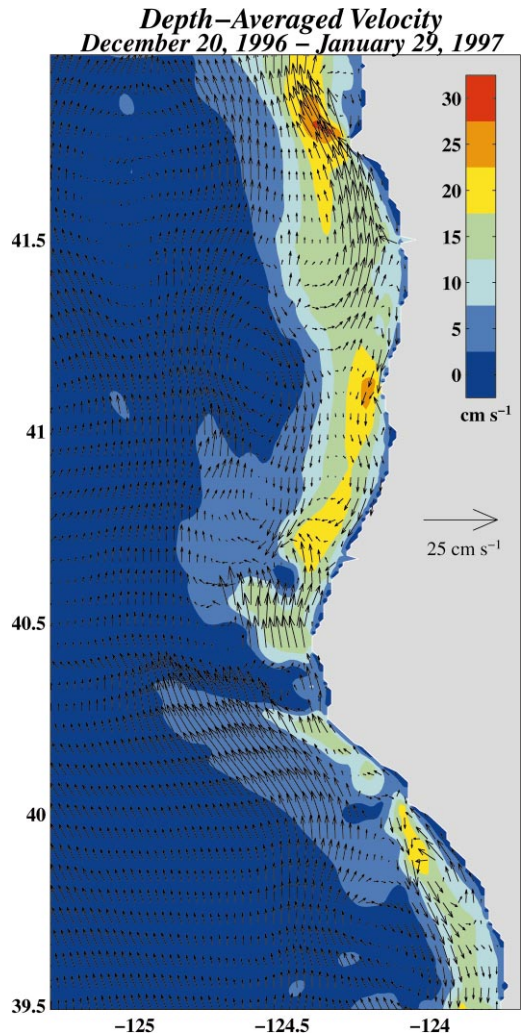


Fig. 6. As in Fig. 5, but for depth-averaged velocity.

coastline morphology, specifically the promontories of Trinidad Head and Point St. George, in enhancing circulation variability in the surface and depth-averaged maps.

4. Time evolution of Eel river plume

Salinity measurements at the G60 site (over the 60 m isobath) during the 40-day simulation period are compared with model quantities in Fig. 7. Salinity measurements from the Seacat sensor are described by Geyer et al. (2000). As in the previous section, the modeled and observed time series consist of inertial

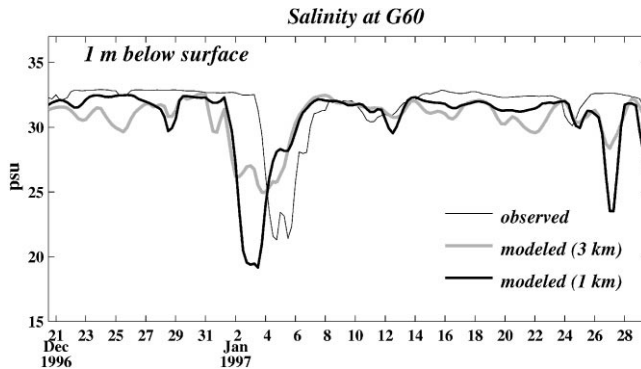


Fig. 7. Observed and modeled near-surface salinity at G60. Salinity measurements are shown courtesy of W.R. Geyer.

averages centered at 6-h intervals. The most prominent feature of the near-surface salinity time series is freshening as the Eel River plume sweeps across the monitoring site. This happens in the models just after the winds rotate to an upwelling-favorable direction. The modeled low-salinity pulse precedes the observed pulse by about a day and a half. The modeled (1 km) river plume expands offshore after January 2 as Eel River discharge peaks (Fig. 8). With the winds providing reduced forcing relative to earlier times, the plume moves offshore on January 2–3 mostly through its own dynamics. Geyer et al. (2000) point out that the axis of the Eel River mouth is rotated about 20° from the alongshore direction. They suggest that this oblique orientation causes the momentum from the Eel River flood to be injected predominantly alongshore (northward) rather than across-shore. In contrast, the model river mouth enters the shelf in the across-shore direction. This may result in a wider plume and account for the earlier appearance of the low-salinity plume signature at G60 in the model. By January 4 the 1-km model plume is advected to the south of the G60 site under the influence of equatorward wind forcing (Fig. 8). The 1-km model salinity anomaly is about 13 psu and is closer to the observed plume in magnitude and duration than the 3-km model.

Temperature at 1 m depth was also measured at the G60 site (Geyer et al., 2000). Modeled fluctuations in near-surface temperature do not match the observed variability. Absolute errors, however, are small. The differences in standard deviation are 0.17° for the 3-km model and -0.03° for the 1-km model. Modeled mean temperature is slightly warmer than the observed mean. The differences in mean values are 0.47° for the 3-km model and 0.29° for the 1-km model.

The time series discussed above supply information at a single location. With an understanding in hand of the model strengths and limitations in reproducing time series observations during the flood, we next examine the model evolution of the across-shelf structure of the plume during the flood as represented by the 1-km model. All variables shown in subsequent sections are averaged over an inertial period.

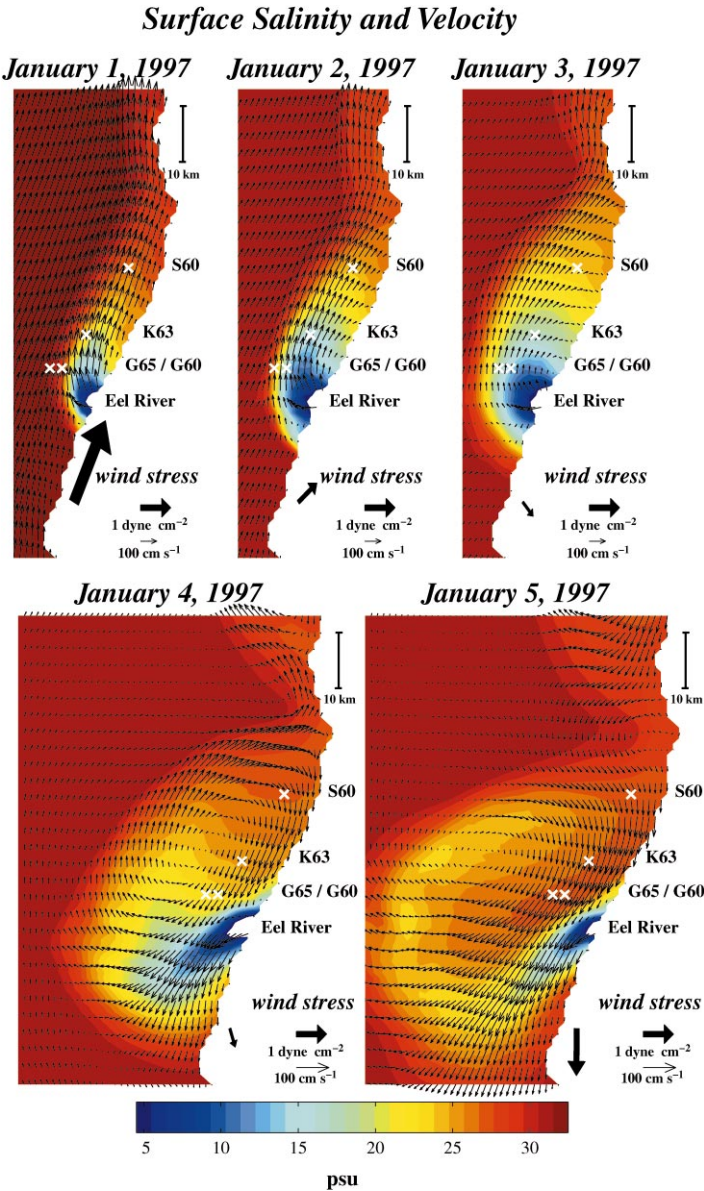


Fig. 8. Time evolution of surface salinity and velocity on the Eel margin. Every third vector is shown in the alongshore direction. Every vector is shown across-shore. STRATAFORM observation sites are indicated with crosses. NOGAPS wind stress at the location of Buoy No. 30 is shown for reference. The velocity scale changes between the upper and lower figures.

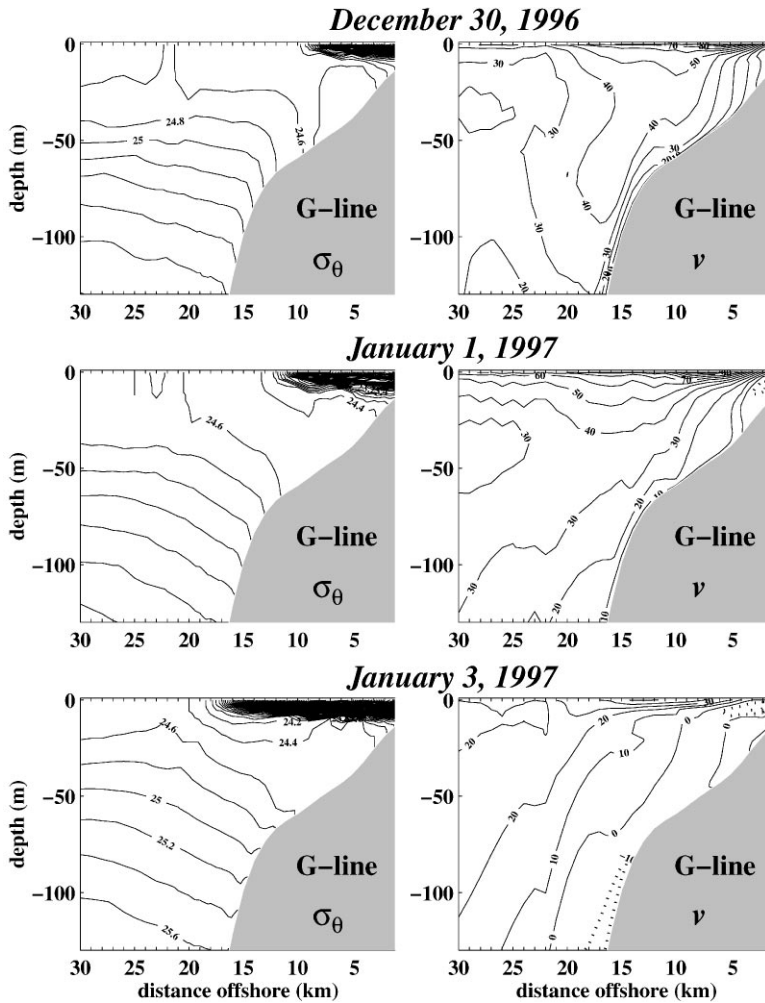


Fig. 9. East–west sections of potential density (σ_θ) and north–south velocity (v) through the STRATAFORM G-line (sites G65 and G60). Units are kg m^{-3} for potential density and for velocity (cm/s). Dotted lines represent southward flow.

Potential density (σ_θ) and north–south velocity (v) on east–west sections extending through G60/G65 (on the G-line), near the mouth of the Eel River (Fig. 9), and through S60 (on the S-line), 18 km to the north (Fig. 10), are highly variable during the course of the Eel River flood. During strong pole-ward winds and in the initial flood stages (December 30) the shelf waters out to about 10 km from the coast are relatively unstratified except for the surface plume. The developing plume is deeper and more bottom-attached on the S-line relative to the G-line. On both sections a poleward coastal jet over the shelf is evident. However, on the S-line the jet is more tightly confined to the shelf than it is on the G-line. Velocity is poleward over most

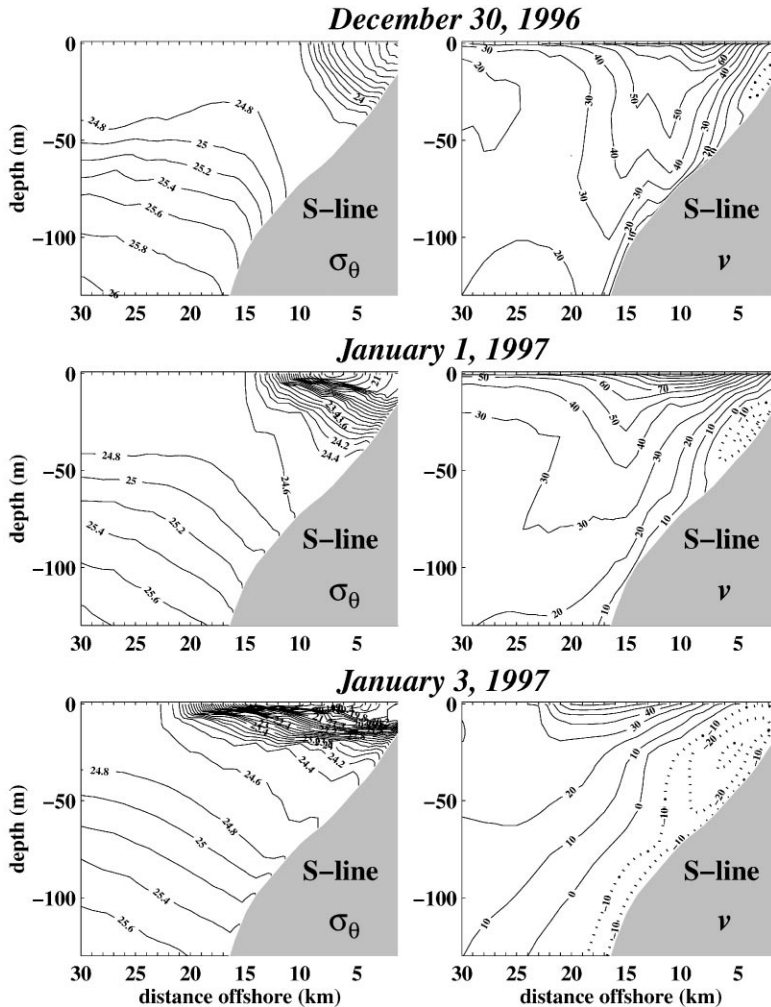


Fig. 10. As Fig. 9, but for east-west sections through the S-line (S60 site).

of the shelf at both sites; yet, there is equatorward flow near the bottom on the S-line inner shelf. During declining poleward winds and near-maximum river discharge (January 1) the plume thickens vertically on both sections. The poleward jet at both sites moves offshore. During equatorward winds and post-peak discharge (January 3), the plume spreads offshore and thins vertically at both sections. Over the outer shelf and shelfbreak the density attempts to restratify at both sections in response to the upwelling-favorable winds. The modeled Eel River plume response to the winds on the S-line and G-line mimics the across-shelf narrowing and vertical thickening (downwelling-favorable winds) replaced by across-shelf spreading and vertical thinning (upwelling-favorable winds) of the plume documented by Geyer et al.

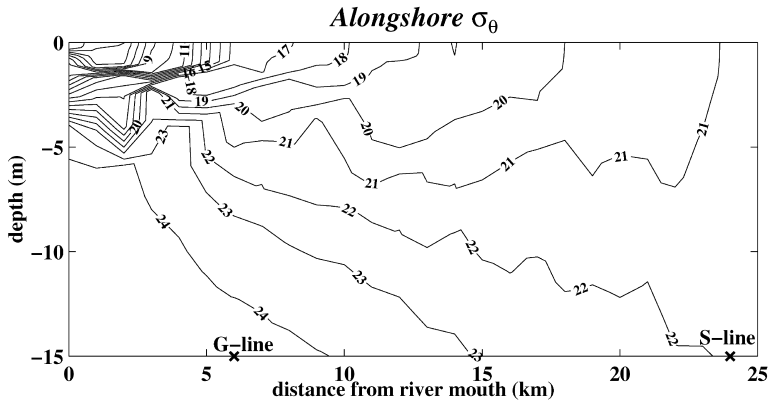


Fig. 11. Alongshore section of potential density (σ_θ) on January 1, 1997 at an offshore distance of 1.5 km from the coast. Units are kg m^{-3} . The section is 25 km long and extends north from the mouth of the Eel River. The locations of the STRATAFORM G-line and S-line are indicated.

(2000) from helicopter-lowered CTD surveys. The flow reversal on the S-line gains strength over time such that by January 3 the flow on the inner shelf is predominantly equatorward. Equatorward flow of smaller magnitude begins to occupy the shelf region on the G-line as well.

An alongshore section of potential density through the plume on January 1 at an offshore distance of 1.5 km from the coast is shown in Fig. 11. Most of the low-density plume water is confined to the upper 5 m. Very light water ($\sigma_\theta < 18 \text{ kg m}^{-3}$) extends about 10 km north of the Eel River mouth in the surface waters. Light water stretching to about 10 km north of the mouth is qualitatively consistent with data from hydrographic surveys by Geyer et al. (2000). The plume deepens as it flows north, leading to the bottom-attachment seen on the S-line (Fig. 10). The thickening of the plume to the north during downwelling-favorable winds was observed by Geyer et al. (2000) during helicopter CTD surveys.

To help clarify the role of vertical turbulent mixing in the physical response of the shelf and plume waters to the applied time-dependent wind forcing, sections along the S-line of gradient Richardson number

$$\text{Ri} = \frac{-g}{\rho_0} \frac{\partial \sigma_\theta}{\partial z} \left[\left(\frac{\partial u}{\partial z} \right)^2 + \left(\frac{\partial v}{\partial z} \right)^2 \right]^{-1} \quad (1)$$

twice the turbulent kinetic energy q^2 from the Mellor and Yamada (1982) level 2.5 turbulence closure scheme, and vertical kinematic diffusivity K_H are displayed in Fig. 12. On December 30 enhanced mixing over the outer shelf is evident in Ri , q^2 , and K_H . Fields of vertical kinematic viscosity K_M are similar to those of K_H . The near vertical contours of q^2 and K_H suggest the position of an outer shelf downwelling front that has developed under persistent strong poleward winds during the preceding days (Allen and Newberger, 1996). Over the inner shelf there is some slightly increased mixing in the upper 30 m. On January 1 as the Eel River discharge

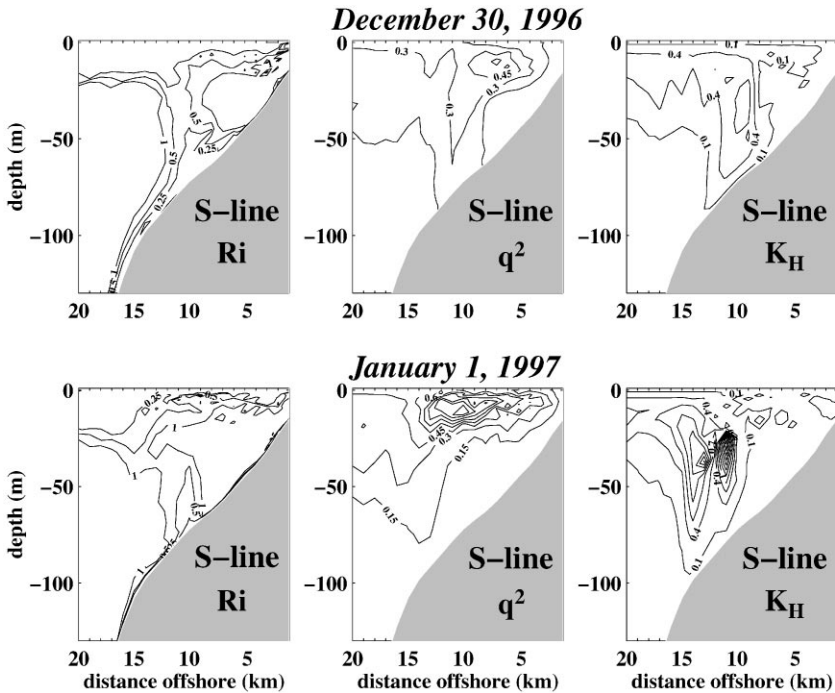


Fig. 12. East–west sections of gradient Richardson number Ri , twice the turbulent kinetic energy q^2 , and vertical kinematic diffusivity K_H along the S-line. Fields are in units of $m^2 s^{-2}$ multiplied by 10^2 for q^2 , and $m^2 s^{-2}$ multiplied by 10 for K_H . Contours of Ri are 1, 0.5, 0.25 and 0.

risers and the winds slacken, increased Ri values on the outer shelf indicate a stabilized water column. Fields of q^2 have increased magnitudes presumably as a result of increased vertical shear near the surface in the alongshore current. The large values of q^2 are not accompanied, however, by large values of K_H . The relatively small values of K_H are caused by the effects of stable stratification in the plume through the structure functions in the Mellor and Yamada (1982) formulation and are suggestive of an absence of significant vertical mixing. An evaluation, discussed below, of the balance of terms in the salinity equation shows, however, that vertical diffusion plays a significant role in determining the structure of the salinity field under the plume as might be anticipated from the large vertical gradients of salinity and the significant wind stress during this time period.

In order to explore the mechanism for plume deepening on the S-line seen in Fig. 10, we partition the salinity equation into the tendency ($\partial S/\partial t$), advection (including both horizontal and vertical advection), and diffusion (including both vertical and horizontal diffusion) terms and plot these on December 30 and on January 1 on an east–west section along the S-line (Fig. 13). Dominant features of the term balance on both days are described here. Relatively large positive values of the advection term near the surface within 15 km of the coast represent the

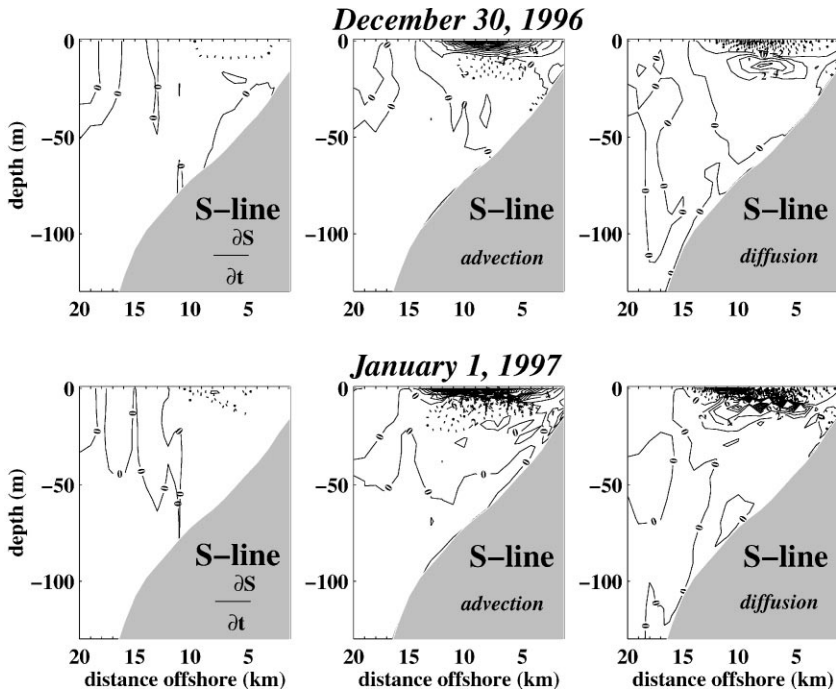


Fig. 13. Dominant terms in the salinity equation on an east–west section through the S-line. The terms are multiplied by 10^5 and units are psu s^{-1} . Negative values are shown with a dotted line.

northward advection of low-salinity plume water by the alongshore current. This is primarily balanced by vertical diffusion, which mixes higher salinity water from below into the near-surface region as indicated by negative values of the diffusion term. Vertical diffusion also mixes low-salinity near-surface water from the plume to depths of 20–30 m as shown by the positive values of the diffusion term. The latter process is primarily balanced by negative advection. Assuming that the dominant contribution to advection is from the alongshore velocity, the change in sign in the advection term near 10 m depth is consistent with the alongshore structure of the potential density in Fig. 11 which shows increasing σ_θ near the surface and decreasing σ_θ below 10 m as the distance increases northward from the river. The relatively small imbalance between advection and diffusion results in a negative tendency term which is largest near the offshore edge of the plume and which represents a net freshening of the near-surface water as the plume increases in strength. An examination of the term balances on an alongshore section 5.5 km from the coast indicates that the processes described above, involving major contributions from both advection and vertical diffusion, occur robustly at alongshore locations between the G-line and S-line from 30 December through 1 January.

By the end of the storm, significant structure has developed in the shelf flow field. Walsh and Nittroer (1999) identified an eddy in advanced very high resolution

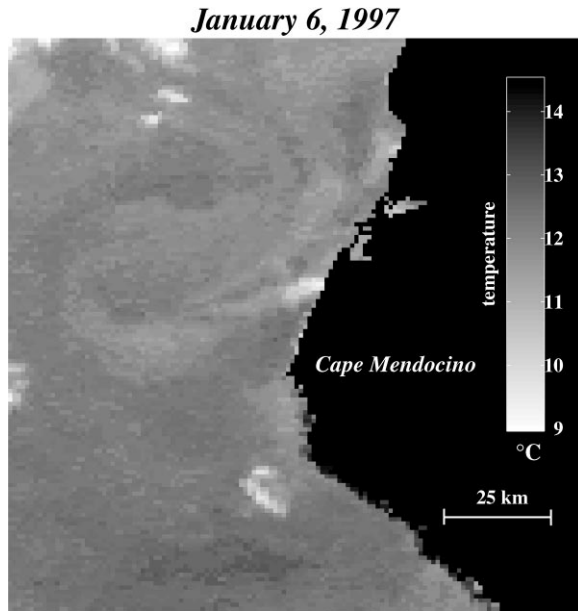


Fig. 14. AVHRR satellite (NOAA-14) image collected by the GLOBEC Northeast Pacific program. Processing of the image was carried out by Ocean Imaging, Inc. The image shows the eddy just north of Cape Mendocino.

radiometer (AVHRR) satellite imagery on January 6, 1997. They interpret the image of the visible band (channel 1) minus the near-infrared band (channel 2) as representative of turbidity. We have found that the eddy is also evident in the far-infrared (channel 4) temperature-corrected (Pathfinder SST algorithm) NOAA-14 satellite data (Fig. 14). The Eel River water is up to several degrees cooler than the ambient shelf water, which provides a thermal signature as the river plume undergoes an anticyclonic wrapping just north of Cape Mendocino. The eddy feature was identified in Pullen and Allen (2000) and found to be a robust response to storm passage, even in the absence of river run-off.

The impact of the shelf circulation on the Eel River plume in the 1-km model simulation is apparent in Fig. 8. During strong poleward winds (January 1) the plume (as delineated by surface salinity) hugs the coast and courses northward with surface velocities on the order of 1 m s^{-1} . As the winds reverse direction through January 2 and 3 the plume spreads offshore. During the period from January 4 to 5, the low-salinity waters from the Eel River are wound clockwise into the developing eddy and move farther offshore. This eddy is approximately 50 km in diameter, in agreement with the size of the eddy imaged by satellite.

The spatial complexity of the bottom flow is highlighted in Fig. 15. Maps of bottom velocity during the storm show weak equatorward flow on January 1 over the inner shelf adjacent to S60. This flow gains strength by January 2 and spreads to the surface waters two days later (Fig. 8). The upward expansion with time of the

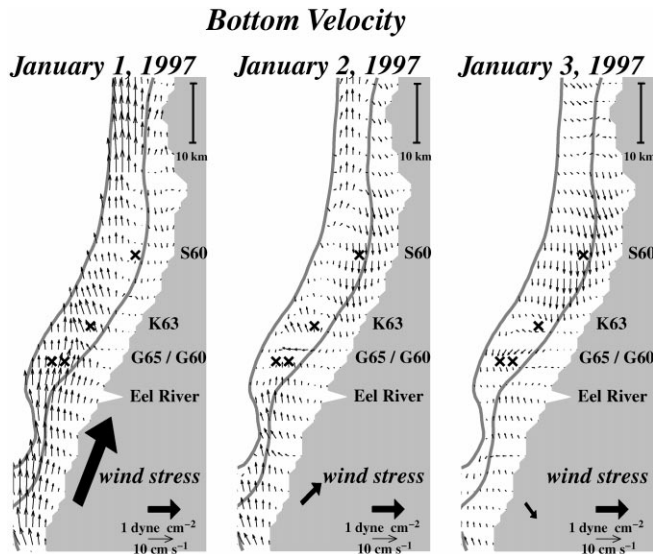


Fig. 15. Time evolution of velocity (cm s^{-1}) on the bottom sigma level during the storm. Every third vector is shown alongshore. Every across-shore vector is shown. The 50 and 100 m isobaths are drawn for reference.

equatorward flow was identified in the S-line sections (Fig. 10). Here, the reversal in bottom currents is found to be localized between the region north of the K63 site and south of Trinidad Head. The establishment of the pressure gradients that are important in forcing the equatorward flow reversal may be seen in the plots of sea-surface elevation in Fig. 16. High sea-surface elevation south of Trinidad Head is a prevalent feature from January 1 to 3. These high sea levels diminish as the eddy takes shape and migrates offshore on January 4 and 5. A comparable 1-km resolution model simulation was conducted with no river run-off to assess the contribution of river run-off to the flow reversal. In that simulation, explored in more detail below, elevated values of sea level still occur south of Trinidad Head, but the magnitudes are reduced by about 5 cm s^{-1} . Without river run-off, a weakened eddy begins to form about a day later than the river-enhanced eddy.

Sections of potential density and north–south velocity along the S-line from the “no rivers” simulation (Fig. 17) are markedly different from the simulation with rivers (Fig. 10). Without rivers the inner shelf waters are well mixed vertically during the storm event. On January 1 the coastal jet is weaker by about 50 cm s^{-1} and positioned farther offshore than the buoyancy-augmented jet. There is a hint of developing equatorward flow on the shelf. However, it lags the strong equatorward flow on January 3 seen in the simulation with rivers (Fig. 10).

A section along the S-line of the north–south pressure gradient with and without rivers (Fig. 18) shows increased negative pressure gradient in the plume near the surface, and increased positive gradients (southward pressure gradient force) inshore

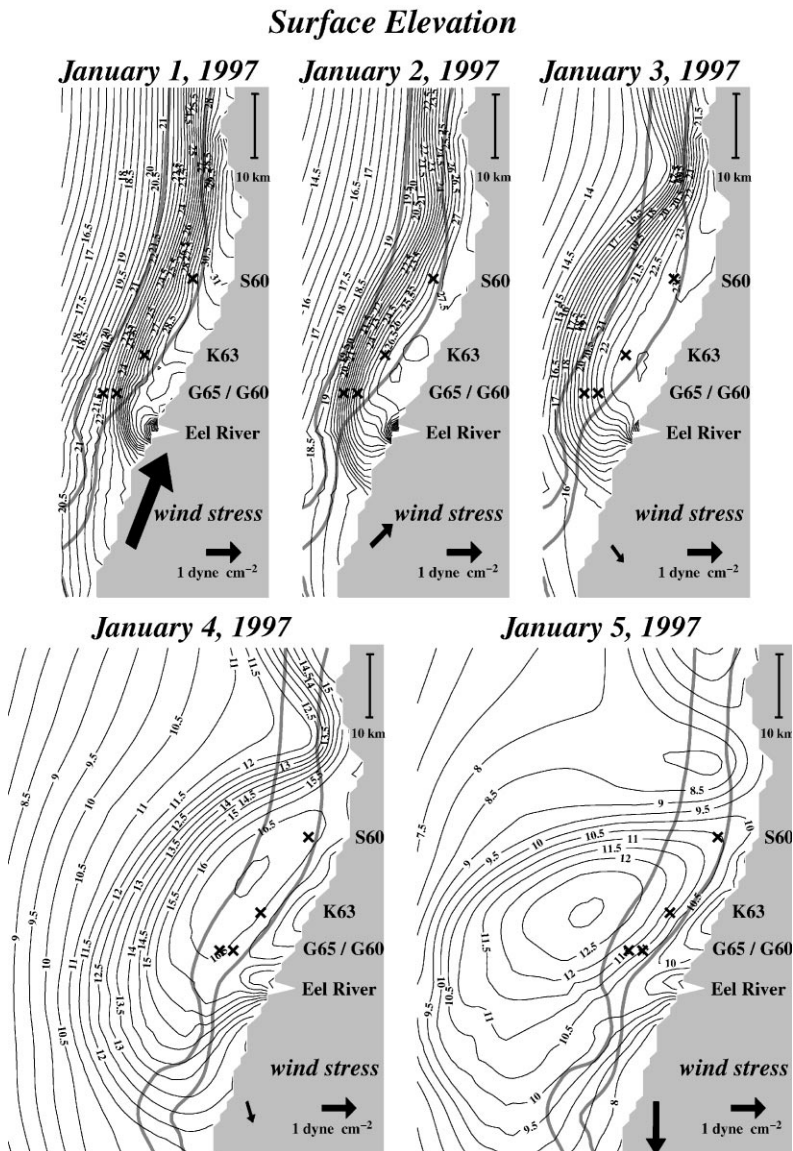


Fig. 16. Time evolution of sea-surface elevation on the Eel margin. Units are cm. Details are as in Fig. 8. The 50 and 100 m isobaths are shown in grey.

compared with the simulation without rivers. The positive pressure gradients on the inner shelf are weak and barotropic without rivers but become stronger and more baroclinic when buoyancy from the river plume is included. The strong equatorward flow on the shelf on the S-line that developed between December 30 and January 1 can be ascribed to pressure gradients set up by the plume.

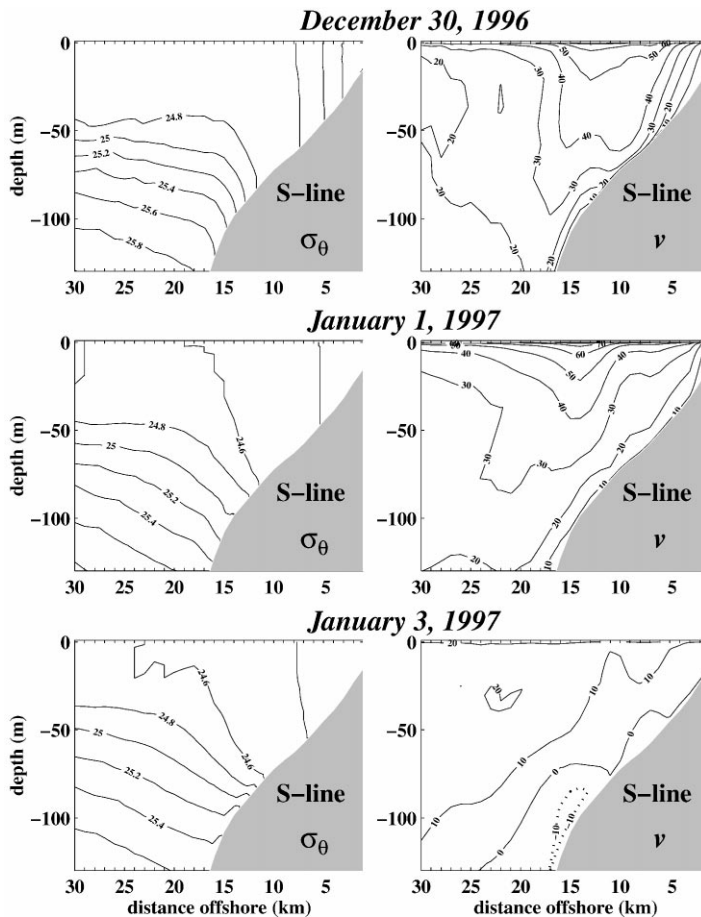


Fig. 17. Same as Fig. 10, but for the simulation without rivers.

Several centimeters of fine-grained sediment accumulated on the 60 m isobath between the sites identified as S60 and G60 in Fig. 15 (Wheatcroft and Borgeld, 2000) as a result of the flood. Ogston et al. (2000) analyzed sediment flux in the bottom boundary layer at the G65, K63 and S60 sites and found convergent flux between S60 and K63. This convergence is consistent with the velocity vectors of Fig. 15. Data from S4 electromagnetic current meters in the bottom boundary layer along the 60 m isobath during the flood event (Ogston et al., 2000) are compared with modeled velocities at the same locations in Table 1. Statistics are computed for a 12-day period surrounding the flood event. In both the modeled and observed data, the K63 site is the locus of largest poleward mean alongshore bottom current as well as largest standard deviation. At G65, the poleward mean flow is weaker and less variable in both modeled and observed time series. At S60, equatorward mean bottom flow leads to convergent bottom currents between S60 and K63 along the 60 m isobath in the model and in the observations.

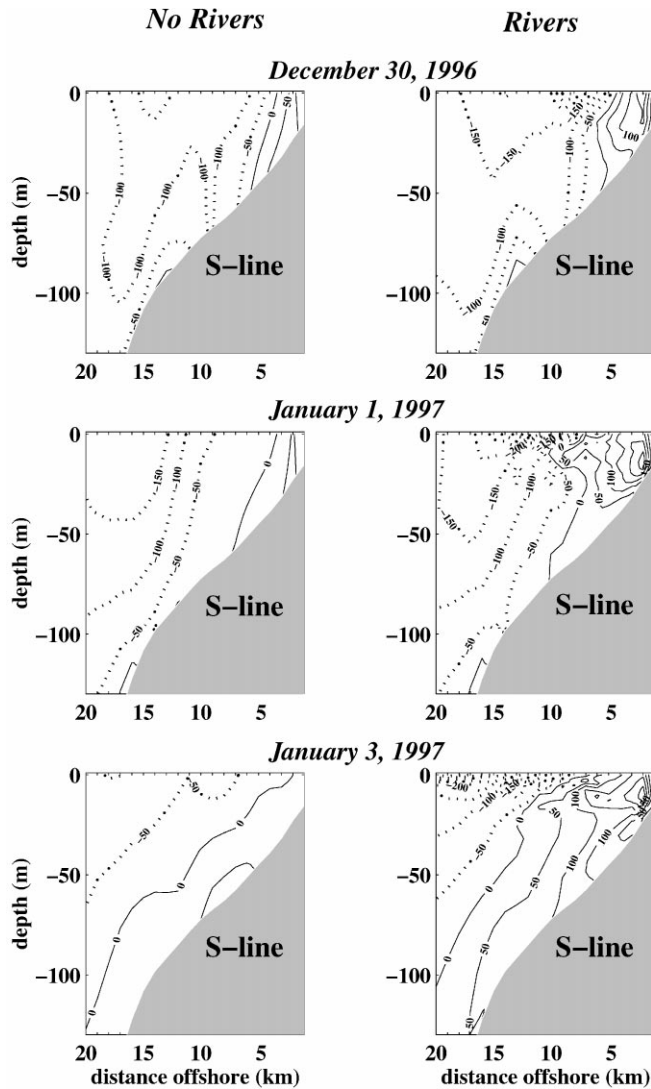


Fig. 18. East-west sections of north-south pressure gradient, $(1/\rho_0)(\partial p/\partial y)$, through the S-line. Sections for the simulation with and without rivers are shown. Pressure gradients are multiplied by 10^7 and units are m s^{-2} .

From helicopter-sampled suspended sediment concentrations in the plume, Geyer et al. (2000) establish that between January 2 and 3 sediment was lost from the plume. In terms of the model results described here, this information implies that sediment is sinking out of the poleward-flowing plume on January 2 into the equatorward flow near the bottom. The sheared flow that the sediment experiences

Table 1

Modeled and observed major axis (alongshore) velocity (cm s^{-1}) time series statistics at STRATAFORM G65, K63, S60 current meter locations approximately 1 m above the seabed (December 25, 1996–January 6, 1997). (Observed data shown courtesy of C. Friedrichs and A. Ogston.)

Major axis velocity	Correlation coeff.	Mean	SD.
Observed S60	0.67	– 3.47	12.89
Modeled		– 1.33	7.87
Observed K63	0.80	12.49	14.58
Modeled		4.78	9.36
Observed G65	0.90	1.04	12.31
Modeled		1.65	6.63

could be important in moving sediment southward of where it might have accumulated if the water below the plume were quiescent.

With regard to classifying the dynamics of the Eel River plume during the flood event, the highly time-dependent behavior resulting from the extreme variability in the wind stress forcing and the river discharge between December 27 and January 6 (Fig. 2) makes meaningful parameter estimation and utilization uncertain. Nevertheless, a calculation and comparison of some relevant instantaneous scales should help provide context. Consequently, we proceed and choose January 2 when the wind stress is relatively weak and the discharge is high (Fig. 8) for some parameter estimates. The Rossby radius of deformation R_D for the first baroclinic mode has been calculated at a number of locations in the plume by using the local stratification and water depth from the model, assuming a flat bottom, and solving the vertical eigenvalue problem. We find $R_D = R_{D_i} \simeq 10.5 \text{ km}$ near the river mouth and $R_D = R_{D_p} \simeq 12\text{--}14 \text{ km}$ in the plume at distances of 4–10 km offshore and 10–15 km north of the river mouth. The corresponding internal wave velocities $c = fR_D$ are $c = c_i \simeq 1 \text{ m s}^{-1}$ near the mouth and $c = c_p \simeq 1.15\text{--}1.33 \text{ m s}^{-1}$ in the plume. From the model results we find that the offshore surface velocity near the river mouth is approximately $u_i \simeq 1.2 \text{ m s}^{-1}$ while the alongshore surface velocities in the plume are typically $v_p \simeq 1 \text{ m s}^{-1}$. The across-shelf scale L_0 of the plume, estimated from the surface salinity field in Fig. 8, is $L_0 \simeq 12 \text{ km}$. With these values, we estimate for January 2 the inlet Froude number $F_i = u_i/c_i \simeq 1.2$, corresponding to weakly supercritical conditions in the inlet, and a plume Froude number $F_p = v_p/c_p \simeq 0.75\text{--}0.87$, corresponding to subcritical flow in the plume. An inertial scale $L_I = u_i/f \simeq 13 \text{ km}$ is close to L_0, R_{D_i} and R_{D_p} . The plume Kelvin number (Garvine, 1995), $K = L_0/R_{D_i} \simeq 1.2$. In addition, the Rossby numbers $\varepsilon_i = u_i/fL_0 \simeq 1.05$ and $\varepsilon_p = v_p/fL_0 \simeq 1.0$. Given the uncertainties inherent in these scale estimates, we feel that the most reasonable conclusion here is that for January 2, the values of parameters $K, L_I/L_0, F_i, F_p, \varepsilon_i$, and ε_p are all of order one. This implies that stratification, rotation, and nonlinear advective effects are all important contributing factors in the dynamical balances of the instantaneous Eel River plume on January 2.

5. Discussion and summary

This study has described results from a 1-km resolution nested model simulation of the northern California margin. The simulation focused on the major Eel River flood event which occurred as a severe storm passed over and generated winds that veered from poleward (downwelling-favorable) to equatorward (upwelling-favorable). High-resolution modeling enables the mapping of statistical properties of flow variables. Such maps of mean and rms fluctuations of currents are valuable tools for characterizing the dynamic coastal ocean. The shelf flow on the northern Eel margin during the 40-day model simulation consists of strong mean poleward surface velocities with rms fluctuations of 50 cm s^{-1} . Modeled depth-averaged time-mean flow is equatorward with rms fluctuations of 20 cm s^{-1} . Though possessing oppositely directed time-mean currents, both surface and depth-averaged flow display enhanced intensity over the northern Eel River margin.

Observed time-mean major axis (alongshore) velocity at S60 is equatorward at all depths, while the observed standard deviation of the alongshore velocity is on average 20 cm s^{-1} in the water column. The 1-km simulation reproduces the vertical structure of the mean alongshore flow over the shelf at S60 better than the 3-km simulation. In agreement with the observations, fluctuations in alongshore and across-shore 1-km model velocity are larger at the G65 site compared to the S60 site. Major axis (alongshore) 1- and 3-km model currents are highly correlated ($0.80 \leq r \leq 0.85$) with observations at G65. Model simulations of minor axis (across-shore) velocities are not as successful, presumably due in part to the short correlation scales of across-shore velocity.

Across-shelf sections during the flood show a near-surface plume advancing onto an extremely well-mixed shelf. Deepening of the plume to the north between the G-line and S-line is a prominent feature of the alongshore plume structure during downwelling-favorable winds. This feature appears to be associated primarily with vertical mixing that is presumably intensified by the large wind stress. Properties of the modeled river plume agree with observations taken during downwelling conditions (Geyer et al., 2000). Under the influence of upwelling-favorable winds the plume thins and stretches offshore. The modeled plume sweeps across the G60 site several days earlier than the observed plume as evidenced by a comparison of salinity time series. This discrepancy may be due to the model river plume being wider since the model inlet geometry constrains the resultant momentum from the river to be input to the shelf in the across-shore direction. The axis of the Eel River mouth, however, is rotated about 20° from the alongshore direction so the river would input momentum northward.

In satellite imagery and model simulations, an anticyclonic eddy forms over the outer shelf as the storm passes and winds shift equatorward. Based on the 3-km model simulation, Pullen and Allen (2000) determined the eddy to be a generic feature of the relaxation response from strong poleward wind forcing during storms, whose circulation is enhanced by river run-off. The low-salinity Eel River plume water becomes entwined in the developing eddy. The onshore limb of the eddy is linked to equatorward flow over the inner shelf. Bottom velocities over the inner

shelf turn equatorward several days before the surface velocities in the 1-km simulation. The equatorward flow over the shelf during the transition of winds from strongly poleward to weakly equatorward is attributed to a southward pressure gradient force that develops south of Trinidad Head during strong poleward winds. This pressure gradient force is both intensified and baroclinic in structure due to the presence of the Eel River plume.

The observed suspended sediment concentrations, sediment flux vectors and sediment accumulation on the 60 m isobath (Geyer et al., 2000; Ogston et al., 2000; Wheatcroft and Borgeld, 2000) may be indicative of sediment leaving the fast northward-flowing plume over the inner shelf, up to 60 km from the river mouth (Geyer et al., 2000), and sinking through a highly sheared water column with southward flow at depth. Convergent bottom currents in the model and observations steer flow to the region between S60 and K63. Hence sediment accumulation patterns may be linked to these low-frequency circulation patterns.

There are many documented instances of persistent circulation features amassing sediments in preferred locations (Dyer and Huntley, 1999). The eddy described here is a transient phenomenon, occurring in response to passing storms. The extent to which the low-frequency circulation could determine the fate of sediment may best be approached by a combined sediment transport/physical circulation model that is cognizant of the major role played by coastline irregularities, wind forcing, and river run-off in determining the shelf response, as demonstrated here.

Acknowledgements

Discussions with W. Rockwell Geyer and Andrea Ogston were important to this work. The assistance of Priscilla Newberger in model implementation is gratefully acknowledged. We thank Corinne James for help with presentation of the satellite data in Fig. 14. Adriana Huyer and two reviewers provided important feedback about the manuscript. This work was supported in part by a grant of Cray C90, T90 and SV1 time from the Department of Defense Major Shared Resource Centers at Wright-Patterson Air Force Base and at the Naval Oceanographic Office. This work was funded by the Office of Naval Research through Grants N00014-93-1-0804, N00014-93-1-1301 and N00014-97-1-0165.

References

- Allen, J.S., Newberger, P.A., 1996. Downwelling circulation on the Oregon continental shelf. Part I: Response to idealized forcing. *Journal of Physical Oceanography* 26, 2011–2035.
- Blumberg, A.F., Mellor, G.L., 1987. A description of a three-dimensional coastal ocean circulation model. In: Heaps, N. (Ed.), *Three-Dimensional Coastal Ocean Models*, Vol. 4. Amer. Geophys. Union, Washington, DC, pp. 1–16.
- Chao, S.Y., 1987. Wind-driven motion near inner-shelf fronts. *Journal of Geophysical Research* 92, 3849–3860.

- Clancy, R.M., deWitt, P.W., May, P., Ko, D.S., 1996. Implementation of a coastal ocean circulation model for the west coast of the United States. *Proceedings of the American Meteorological Society Conference on Coastal Oceanic and Atmospheric Prediction*, Atlanta, GA, pp. 72–75.
- Dyer, K.R., Huntley, D.A., 1999. The origin, classification and modelling of sand banks and ridges. *Continental Shelf Research* 19, 1285–1330.
- Fong, D.A., 1998. Dynamics of freshwater plumes: observations and numerical modeling of the wind-forced response and alongshore freshwater transport. Ph.D. dissertation, WHOI/MIT Joint Program, 172 pp.
- Garvine, R.W., 1995. A dynamical system for classifying buoyant coastal discharges. *Continental Shelf Research* 15, 1585–1596.
- Garvine, R.W., 1999. Penetration of buoyant coastal discharge onto the continental shelf: a numerical model experiment. *Journal of Physical Oceanography* 29, 1892–1909.
- Geyer, W.R., Hill, P., Milligan, T., Traykovski, P., 2000. The structure of the Eel River plume during floods. *Continental Shelf Research* 20, 2067–2093.
- Hill, P.S., Milligan, T.G., Geyer, W.R., 2000. Controls on effective settling velocity of suspended sediment in the Eel River flood plume. *Continental Shelf Research* 20, 2095–2111.
- Kourafalou, V.H., 1999. Process studies on the Po River plume, North Adriatic Sea. *Journal of Geophysical Research* 104, 29963–29985.
- Kourafalou, V.H., Oey, L.-Y., Wang, J.D., Lee, T.L., 1996. The fate of river discharge on the continental shelf. 1: Modeling the river plume and the inner shelf coastal current. *Journal of Geophysical Research* 101, 3415–3434.
- Masson, D., Cummins, P.F., 1999. Numerical simulations of a buoyancy-driven coastal countercurrent off Vancouver Island. *Journal of Physical Oceanography* 29, 418–435.
- Mellor, G.L., Yamada, T., 1982. Development of a turbulence closure model for geophysical fluid problems. *Review of Geophysics and Space Physics* 20, 851–875.
- Münchow, A., Garvine, R.W., 1993. Buoyancy and wind forcing of a coastal current. *Journal of Marine Research* 51, 293–322.
- Nittrouer, C.A., 1999. STRATAFORM: overview of its design and synthesis of its results. *Marine Geology* 154, 3–12.
- Ogston, A.S., Cacchione, D.A., Sternberg, R.W., Kineke, G.C., 2000. Observations of storm and river flood-driven sediment transport on the northern California continental shelf. *Continental Shelf Research*, this volume.
- Pullen, J.D., 2000. Modeling studies of the coastal circulation off northern California. Ph.D. Dissertation, Oregon State University.
- Pullen, J.D., Allen, J.S., 2000. Modeling studies of the coastal circulation off northern California: statistics and patterns of wintertime flow. in preparation.
- Rennie, S.E., Largier, J.L., Lentz, S.J., 1999. Observations of a pulsed buoyancy current downstream of Chesapeake Bay. *Journal of Geophysical Research* 104, 18227–18240.
- Sommerfeld, C.K., Nittrouer, C.A., 1999. Modern accumulation rates and a sediment budget for the Eel shelf: a flood-dominated depositional environment. *Marine Geology* 154, 227–241.
- Syvitski, J.P., Morehead, M.D., 1999. Estimating river-sediment discharge to the ocean: application to the Eel margin, northern California. *Marine Geology* 154, 13–28.
- Walsh, J.P., Nittrouer, C.A., 1999. Observations of sediment flux to the Eel continental slope, northern California. *Marine Geology* 154, 55–68.
- Wheatcroft, R.A., Borgeld, J.C., 2000. Large-scale distribution and small-scale properties of oceanic flood deposits on the Eel River shelf. *Continental Shelf Research*, this volume.